AGU PUBLICATIONS

Geophysical Research Letters

RESEARCH LETTER
10.1002/2016GL068674

Key Points:
- Joint analysis of seismic and regional tsunami observations significantly improves the slip model for the 2015 Illapel, Chile, earthquake
- The rupture is shown to have spread unilaterally to the north rather than bilaterally over the entire aftershock zone
- Slip of up to 10 m occurred in the offshore region, with lower slip downdip where the 1943 rupture appears to have occurred

Supporting Information:
- Supporting Information S1

Correspondence to:
K. F. Cheung,
cheung@hawaii.edu

Citation:
Li, L., T. Lay, K. F. Cheung, and L. Ye (2016), Joint modeling of teleseismic and tsunami wave observations to constrain the 16 September 2015 Illapel, Chile, M_w 8.3 earthquake rupture process, *Geophys. Res. Lett.*, *43*, 4303–4312, doi:10.1002/2016GL068674.

Received 15 MAR 2016
Accepted 19 APR 2016
Accepted article online 20 APR 2016
Published online 7 MAY 2016

Joint modeling of teleseismic and tsunami wave observations to constrain the 16 September 2015 Illapel, Chile, M_w 8.3 earthquake rupture process

Linyan Li[1], Thorne Lay[2], Kwok Fai Cheung[1], and Lingling Ye[3]

[1]Department of Ocean and Resources Engineering, University of Hawai'i at Mānoa, Honolulu, Hawaii, USA, [2]Department of Earth and Planetary Sciences, University of California, Santa Cruz, California, USA, [3]Seismological Laboratory, California Institute of Technology, Pasadena, California, USA

Abstract The 16 September 2015 Illapel, Chile, M_w 8.3 earthquake ruptured ~170 km along the plate boundary megathrust fault from 30.0°S to 31.6°S. A patch of offshore slip of up to 10 m extended to near the trench, and a patch of ~3 m slip occurred downdip below the coast. Aftershocks fringe the large-slip zone, extending along the coast from 29.5°S to 32.5°S between the 1922 and 1971/1985 ruptures. The coseismic slip distribution is determined by iterative modeling of teleseismic body waves as well as tsunami signals recorded at three regional DART stations and tide gauges immediately north and south of the rupture. The tsunami observations tightly delimit the rupture length, suppressing bilateral southward extension of slip found in unconstrained teleseismic-wave inversions. The spatially concentrated rupture area, with a stress drop of ~3.2 MPa, is validated by modeling DART and tide gauge observations in Hawaii, which also prove sensitive to the along-strike length of the rupture.

1. Introduction

The expanded availability of high-quality tsunami recordings from DART stations and tide gauges is having a major impact on studies of large plate boundary megathrust earthquakes. Underthrusting events in subduction zones often have significant coseismic slip offshore, which results in strong tsunami excitation. The low speed of tsunami waves enhances their sensitivity to the spatial extent of earthquake-induced seafloor deformation. The recorded waveforms are effective in constraining seaward and along-strike extents of fault displacement that significantly augment the resolution provided by land-based geodetic and seismic observations [e.g., *Lay et al.*, 2011; *Saito et al.*, 2011; *Yamazaki et al.*, 2011b, 2013; *Yokota et al.*, 2011; *Satake et al.*, 2013; *An et al.*, 2014; *Yue et al.*, 2014a, 2014b; *Bai et al.*, 2014; *Heidarzadeh et al.*, 2016; *Yoshimoto et al.*, 2016].

A great earthquake ruptured the plate boundary in central Chile offshore of Illapel on 16 September 2015 along the region of the 1943 (M_s 8.1), 1880, and 1730 events [e.g., *Kelleher*, 1972; *Nishenko*, 1985; *Beck et al.*, 1998]. The source region as shown in Figure 1 is located between the 1971 (M_s 7.9), 1985 (M_w 8.0), and 1906 (M_s 8.3) Valparaíso events to the south [*Comte et al.*, 1986] and the 1922 (M_s 8.3) event to the north [*Beck et al.*, 1998]. The U.S. Geological Survey National Earthquake Information Center (USGS-NEIC) determined a hypocenter for the 2015 Illapel earthquake at 31.573°S, 71.674°W, and 22.4 km deep with an origin time of 22:54:32.9 UTC [http://earthquake.usgs.gov/earthquakes/eventpage/us20003k7a-scientific_origin]. The final global centroid moment tensor (gCMT) solution has a best double-couple mechanism with a shallow-dipping thrust fault [http://www.globalcmt.org/CMTsearch.html]. The gCMT solution has 7° strike, 19° dip, 109° rake, and seismic moment of 3.23×10^{21} Nm (M_w 8.3) at a centroid depth of 17.4 km, with a centroid time shift of 50 s.

The 2015 Illapel earthquake is of particular note because rapid seismological quantification of the event prompted tsunami warning and evacuation notifications within 8 to 11 min of the origin time, resulting in large-scale evacuation along the Chile coast. Shaking damage was extensive, and tsunami runup was about 3 to 6 m along the adjacent coast from 29°S to 32°S, with localized peak values of 13 m at La Cebada (30.98°S, 71.65°W) and 10.8 m at Totoral (30.37°S, 71.67°W) and a tide gauge peak recording of 4.5 m at Coquimbo to the north [*Aránguiz et al.*, 2016; *Contreras-López et al.*, 2016]. Due to the low local population density, the early tsunami warning, and rapid societal response to the evacuation notice, the loss of life was limited to 13 fatalities, with 6 missing.

Several rapid determinations of finite-fault slip distributions were performed for the event (e.g., USGS-NEIC: http://earthquake.usgs.gov/earthquakes/eventpage/us20003k7a#scientific_finitefault; Earth Observatory of

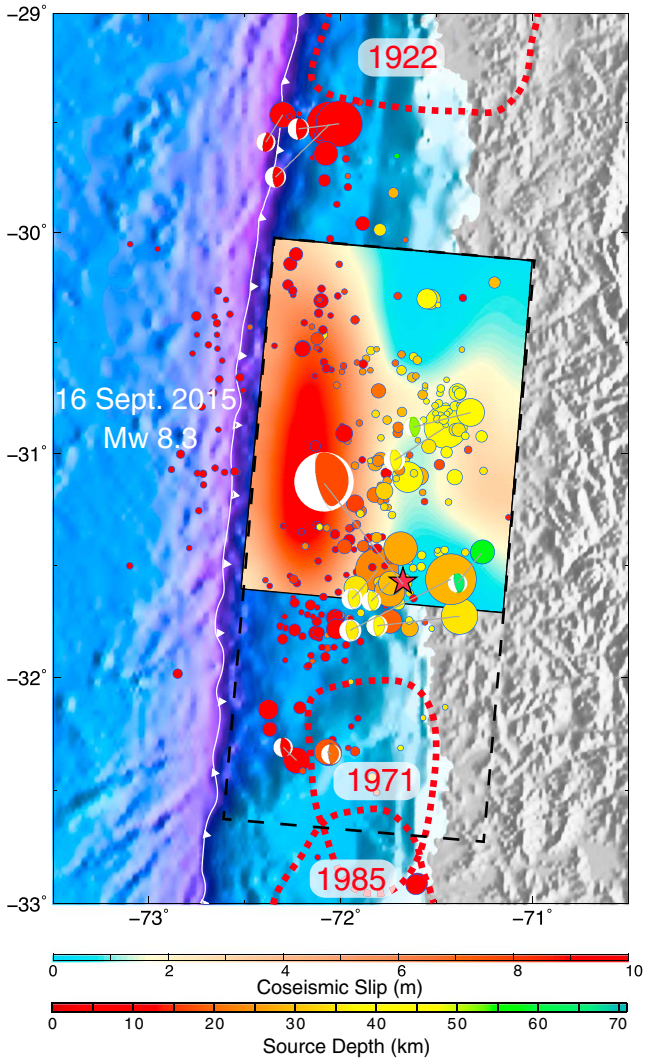

Figure 1. Map of the final slip distribution (blue-red palette) and original model extent (black dashes) with aftershocks from NEIC and CMT solutions and historic event locations. Rupture zones of the adjacent 1922, 1971, and 1985 events are indicated. USGS NEIC seismicity with $m_b \geq 4.5$ from 16 September 2015 to 16 November 2015 is shown by circles, scaled proportional to magnitude and color coded for source depth. Centroid moment tensors for $M_w \geq 6.0$ for the same 2 months are shown by focal mechanisms color coded for centroid depth, plotted at their centroid locations, with tie bars to corresponding NEIC epicenters. The mainshock epicenter is the red star (NEIC value).

Singapore (EOS): http://www.earthobservatory.sg/news/september-16-2015-chile-earthquake; [*Ye et al.*, 2016]). These rapid solutions, which used teleseismic waves only, all locate the region of largest slip northwestward and offshore from the epicenter but with several meters of offshore bilateral slip extending southwestward. Early aftershocks include a concentration of relatively large events ($M_w \sim 6.2$) near 32.3°S, as illustrated in Figure 1, further suggesting the possibility of bilateral rupture. *Ye et al.* [2016] explore the limited resolution of teleseismic-only inversions and present slip models for varying choices of rupture velocity and fault geometry, with all models having some bilateral slip distribution if the parameterization allowed it. *Melgar et al.* [2016] invert geodetic, tide gauge, and strong motion observations and find patches of ~10 m slip beneath the coast and offshore to the north with minor slip near 32°S far offshore.

Teleseismic *P* waves recorded across North America have been analyzed to determine the space-time history of high-frequency seismic energy radiation for the 2015 Illapel earthquake [*Melgar et al.*, 2016; *Ye et al.*, 2016; *Yin et al.*, 2016]. These studies consistently indicate bursts of high-frequency radiation migrating NW and NE from the hypocenter for about 50 s, with extension of lower frequency radiation offshore toward the trench for an additional 40 s. Associated rupture velocities are about 1.5 to 2.0 km/s, although intervals of both slower and faster rupture expansion are suggested. Very little high-frequency radiation is imaged to the south of the hypocenter.

Tsunami observations for the 2015 Illapel earthquake have also been analyzed. *Tang et al.* [2016] discuss the rapid analysis of tsunami signals involved in the Pacific tsunami warning system. *Heidarzadeh et al.* [2016] invert teleseseismic data for a range of assumed rupture velocity and evaluate the fit to DART and tide gauge observations for each case, finding a preferred rupture velocity of 1.75 km/s, with an average of 5 m slip in an offshore patch northwest of the epicenter. *Aranguiz et al.* [2016] use a slip model obtained from teleseismic *P* wave inversion to predict tsunami runup along the coast, matching the 3–6 m runup pattern. In this study, we iteratively model teleseismic and regional tsunami observations, seeking a self-consistent model that improves on seismic-only inversions. Validation of the final model is performed using the far-field tsunami recordings in Hawaii, which are known to be sensitive to slip distributions of trans-Pacific tsunamis due to multiscale resonance along the island chain [*Munger and Cheung*, 2008; *Cheung et al.*, 2013].

2. Iterative Modeling Approach

Our iterative procedure has proved successful in achieving self-consistent rupture models for teleseismic and tsunami observations for numerous events [e.g., *Lay et al*., 2011, 2013a, 2013b; *Yamazaki et al*., 2011b, 2012; *Bai et al*., 2014; *Yue et al*., 2014a]. Global broadband seismic waves are inverted for a kinematic multitime window, finite-source model using a least squares procedure for specified fault geometry and rupture velocity [e.g., *Hartzell and Heaton*, 1983; *Kikuchi and Kanamori*, 1982]. The half-space model of *Okada* [1985] provides the seafloor displacement and velocity for the slip distribution that in turn define the input to the tsunami code NEOWAVE of *Yamazaki et al*. [2009, 2011a] for forward calculations. The staggered finite difference code builds on the nonlinear shallow-water equations with a vertical velocity term to account for weakly dispersive waves and a momentum conservation scheme to describe bore formation. The vertical velocity term also accounts for the time variation of the seafloor vertical motions and facilitates dispersion of the seafloor excitation over the water column during tsunami generation. The method of *Tanioka and Satake* [1996] approximates the vertical motion contributions from seafloor horizontal displacement on a slope.

Our teleseismic data comprise 60 *P* wave and 42 *SH* wave ground displacements filtered in the 0.005–0.9 Hz band. The models discussed here are uniform along a fault strike of 5° but can accommodate variable dip of the plate interface. The subfaults are 22 km along strike and 15 km along dip. The model grid extends from 30°S to 32.6°S (Figure 1), allowing bilateral rupture over up to 13 along-strike segments or unilateral northward rupture on 8 segments. The number of subfaults in the dip direction is set at 9. The subfault source time functions are parameterized with five to seven 3 s rise-time symmetric triangles, offset by 3 s each. The hypocentral depth is set at 26 km, and a wide range of constant and along-dip varying rupture velocities from 1.0 to 3.5 km/s was explored.

Tide gauges along the Chile coast and the Hawaiian Islands as well as DART stations across the Pacific recorded clear signals of the tsunami. Figure 2 shows systems of computational grids to capture signals at selected water-level stations with appropriate resolution. The iterative computations of the regional DART and local tide gauge data utilize two levels of two-way nested grids. Grid 1.1 covers the southeastern Pacific with 2 arc min (~3600 m) resolution, while grids 2.1 and 2.2 resolve the source and the adjacent coasts at 0.5 arc min (~900 m). The nested systems can adequately describe the DART data for adjustment of the source parameters but, due to limited resolution, can only provide qualitative results at the tide gauges for evaluation of arrival time. The far-field model validation is performed with up to five levels of nested grids telescoping from grid 1.2 with 2 arc min (~3600 m) resolution across the Pacific to grid 2.3 with 24 arc sec (~720 m) along the Hawaiian Islands chain, where DART 51407 is located, and to the finest grids with 0.3 arc sec (~9 m) at the tide gauges inside the five commercial harbors. The bathymetry in the computational grids consists of the GEBCO (General Bathymetric Chart of the Oceans) data set at 30 arc sec (~900 m) across the Pacific Ocean and multibeam and lidar survey data at 50 and 3 m resolution around the Hawaiian Islands. A Manning number of 0.035 describes the subgrid roughness of the volcanic and reef substrate in Hawaii [*Bretschneider et al*., 1986].

3. Matching of Seismic and Tsunami Records

We began the iterative procedure using the suite of rapidly determined slip distributions discussed in *Ye et al*. [2016]. The tsunamis computed from these models do not match the records from the three regional DARTs. Models with slip north of 30°S produce early arrivals, and those with concentrated slip very near the trench give a double-peaked initial wave from coastal reflections. Searching over a range of planar fault models showed that those with desired seafloor motions did not match the plate geometry. We thus constructed a variable-dip fault model extending from the trench axis to below the coast conforming with the Slab 1.0 model of *Hayes et al*. [2012] on average. An extensive search over an acceptable range of rupture velocity established suitable offshore placement of fault slip to match the arrival times of the DART recordings. The favored models have a rupture velocity of 3 km/s on the fault deeper than the hypocenter. At shallower depth, the rupture velocity is 3 km/s in the along-strike direction versus 1.0 to 1.5 km/s along dip. The fit to the teleseismic data for all of the models was very good, typically accounting for 80% or more of the power of the observed waveforms, so the primary discrimination among models is based on the corresponding predictions of the DART signals.

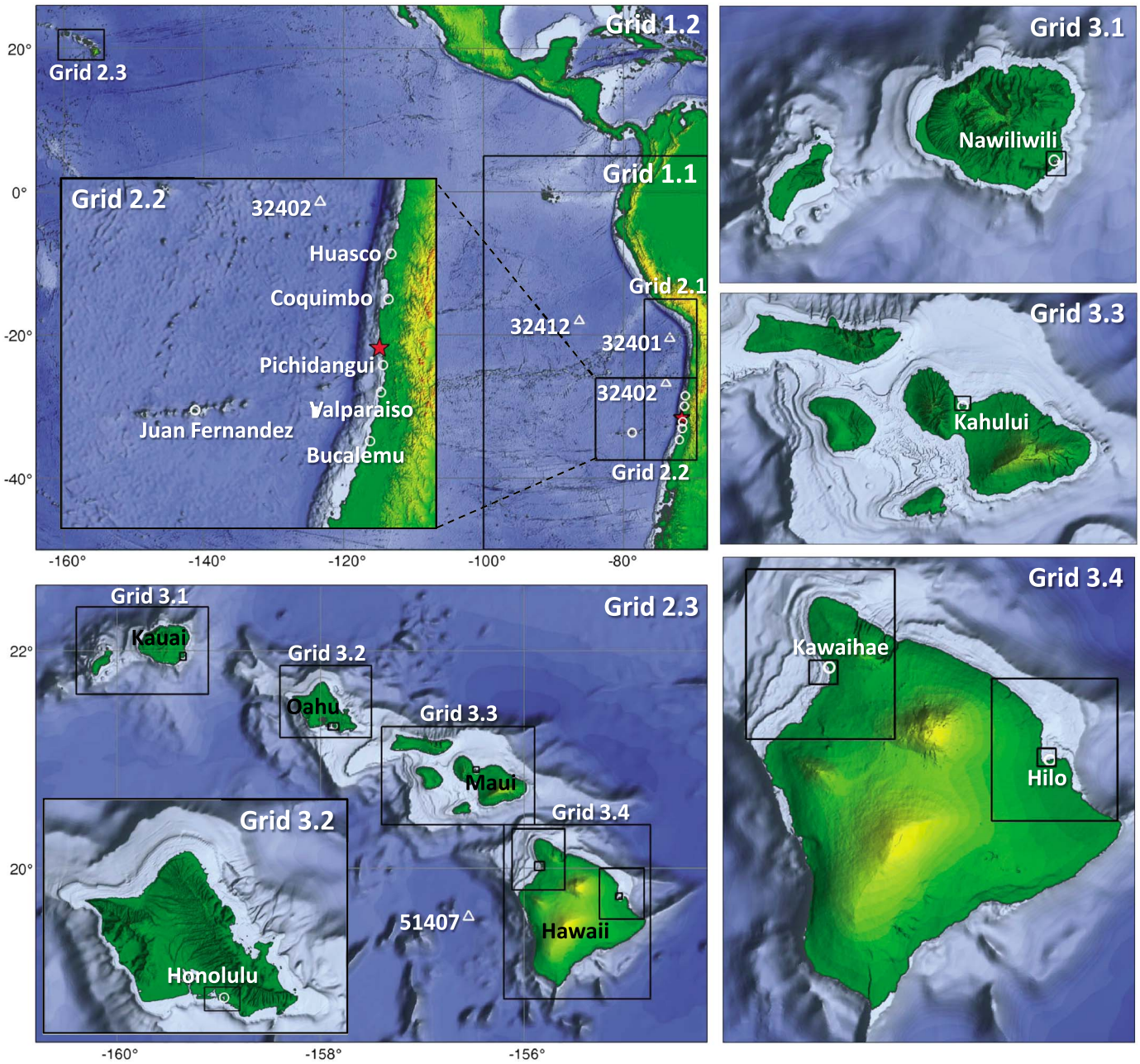

Figure 2. Location maps and arrangement of computational grids for tsunami modeling. The iterative modeling of the regional tsunami was performed with nested grids 1.1 and 2.1 and grids 1.1 and 2.2 separately. The far-field results are provided by nested systems from grids 1.2 to 2.3 across the Pacific Ocean and then the hierarchy of grids from the insular shelves to the harbors of interest as outlined by black regular boxes. The red star denotes the epicenter, and open triangles and circles indicate locations of DART stations and tide gauges, respectively.

A satisfactory fit to the three regional DART observations and the teleseismic data was initially found for a model with substantial bilateral slip from the hypocenter at 31.6°S extending from 30°S to 32.6°S (Figure S1 in the supporting information). The computed tsunami matches both the timing and amplitude of the DART signals. The arrival times at the local tide gauges confirm the northern limit of the rupture but are systematically too early at those to the south of the epicenter (Figure S2). Similar misfit of tide gauge signals was also found by *Heidarzadeh et al.* [2016] for a model with significant bilateral slip. The computed waveforms generally matched the amplitude of the DART and tide gauge records in Hawaii albeit with an increasing phase shift over time due to overestimation of long-period components (Figure S3). Fitting of just the regional DART records does not

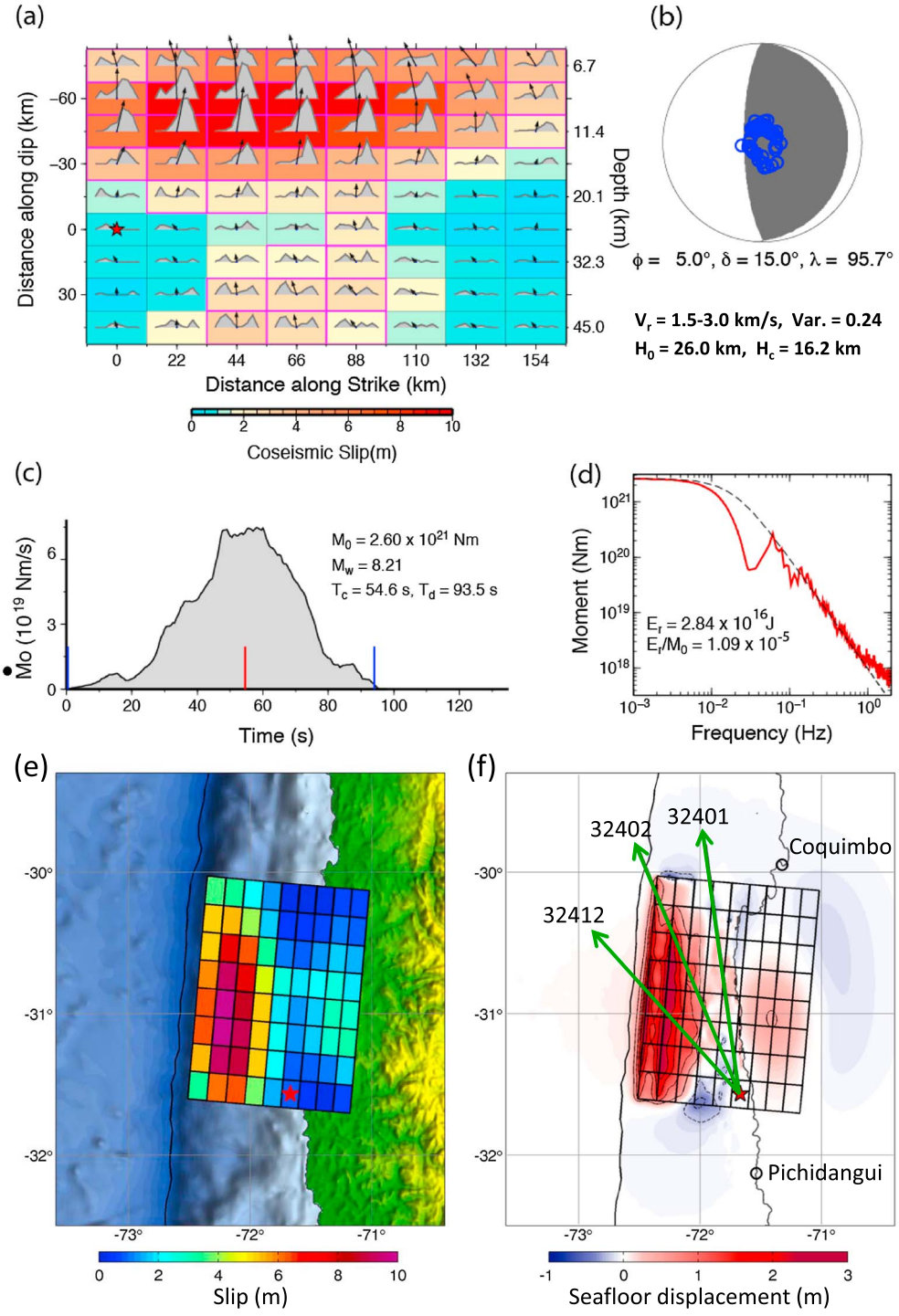

Figure 3. The preferred model of the 2015 Illapel earthquake. (a) Rupture mechanism showing total slip (colors and relative vector lengths), average slip direction (vector directions), and moment rate functions for each subfault. (b) Average focal mechanism, with strike φ, dip δ, and rake λ. V_r is rupture velocity, Var. is residual waveform power mismatch, H_0 is hypocentral depth, and H_c is slip centroid depth. (c) Moment rate function for the finite-fault model with values of seismic moment M_0, moment magnitude M_w, centroid time T_c, and total duration T_d. (d) Average source spectrum from the moment rate function for frequencies < 0.05 Hz and logarithmic average of propagation-corrected P wave displacement spectra for frequencies ≥ 0.05 Hz. E_r is radiated energy. (e) Rupture model in geographic position. The red star indicates the epicenter and the black line denotes the trench. (f) Seafloor uplift and subsidence. Open circles indicate tide gauge locations, and green azimuthal lines point toward the three regional DART stations.

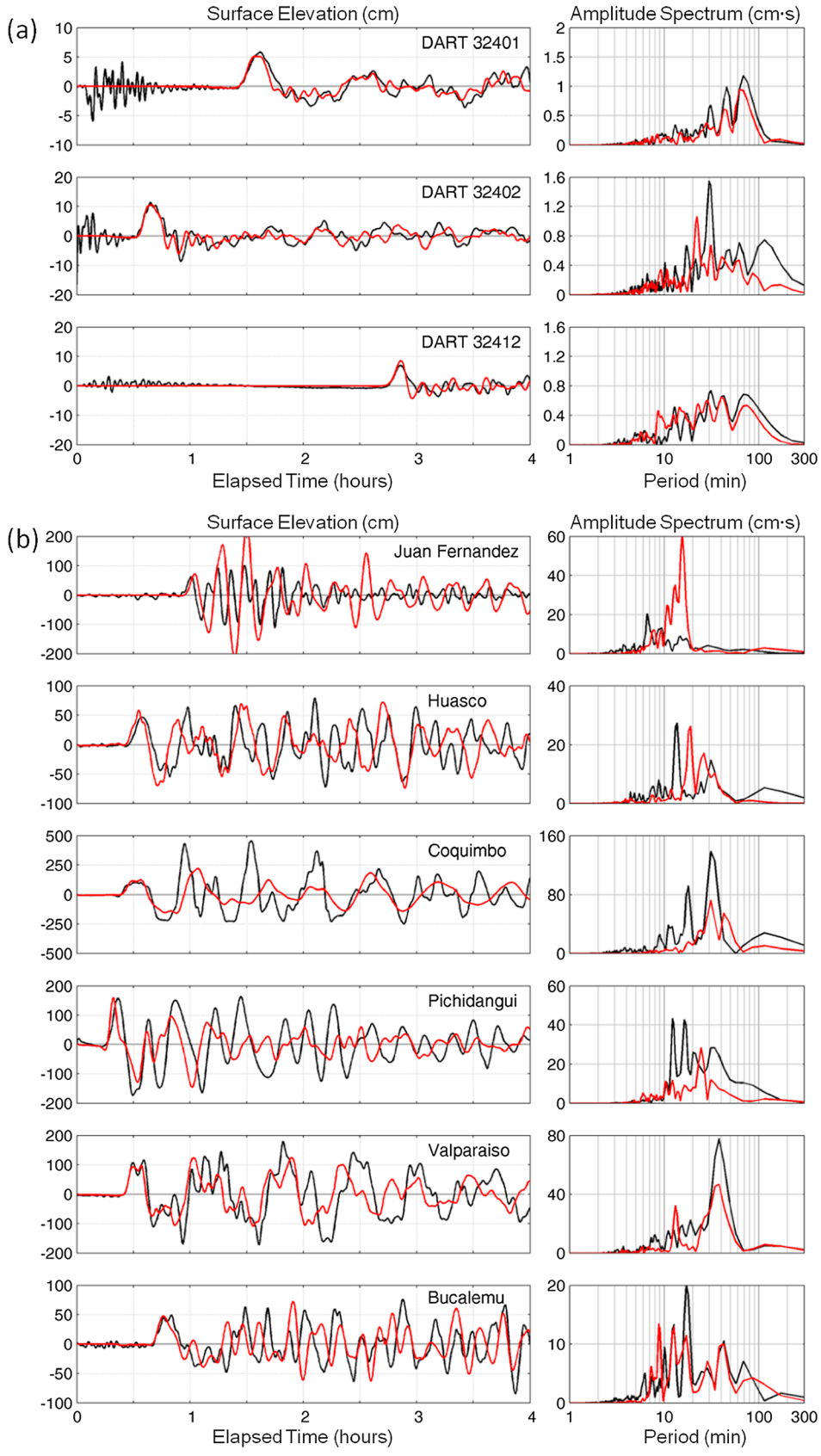

Figure 4

sufficiently constrain the southerly rupture extent because of their limited azimuthal distribution in the northwestern quadrant.

Exploration of the along-strike length, rupture velocity, and subfault duration parameterization ultimately achieved the preferred joint model shown in Figure 3. The unilateral northward rupture has 2.6×10^{21} Nm (M_w 8.21) seismic moment and 93.5 s total duration. Suppression of even modest amounts of slip south of the hypocenter is necessary to avoid predicting early tsunami arrivals to the south (see Figures S4 and S5). The model has a relatively smooth offshore slip distribution with large-slip extending to the trench spanning a 60 km wide portion of the shallow fault. Peak slip is about 10 m, and the subfaults have total allowed rupture durations of 24 s, with subfault moment rate functions similar to the overall moment rate function. The variable rupture velocity is crucial in the placement of the offshore slip to match the arrival times and waveforms at the regional DART stations and local tide gauges (see Figures S6 and S7). There is little slip near the hypocenter, consistent with the slow growth of the teleseismic *P* wave displacements. About 76% of the teleseismic waveform power is accounted for by this model, somewhat less than for bilateral slip models with more degrees of freedom. A downdip patch of several meter slip extends from 30 to 95 km north of the hypocenter with shorter duration pulses in the subfault moment rate functions. A downdip patch below the coast is apparent in the geodetic inversion by *Melgar et al*. [2016], although they find larger slip of about 10 m. High-frequency radiation from this region is imaged by the backprojection studies noted above.

The tsunami records near the source provide the key constraints on the slip distribution. Figure 4 compares the computed and recorded signals at the regional DART stations and local tide gauges. The DART data provide constraints on the northern boundary of the rupture and to a certain extent the updip slip distribution. The model gives slightly high amplitude at DART 32412, while it slightly underestimates the records at 32401. This is acceptable given the assumptions in the NEOWAVE formulation and the model parameterization and is consistent among all models we have tested including those with bilateral slip (see Figures S2 and S5). The weak secondary arrivals from coastal reflection are reasonably well matched, especially the strong negative wave at DART 32402. The comparisons at the tide gauges show good agreement of the arrival time and amplitude of the first wave. The subsequent arrivals, which primarily originate from edge waves along the continental and insular shelves [*Yamazaki and Cheung*, 2011], are not well reproduced by the model because of the low-resolution bathymetry available.

The interconnected insular shelves of the Hawaiian Islands host a series of multiscale resonance modes that amplify the frequency components of tsunamis for evaluation [*Cheung et al*., 2013]. Figure 5 compares the results of the preferred model with records from the DART station and five tide gauges in Hawaii (see Figure 2 for location map). The recorded waveforms vary along the island chain due to dominance of local resonance modes. The model captures these local processes including the 33-and 46-fold increases of the wave height from DART 51407 to the Kahului and Hilo tide gauges. The initial waves at the various locations are well matched by the model after adjustment for travel time shifts associated with neglecting solid earth elasticity and water density variations [e.g., *Tsai et al*., 2013; *Watada et al*., 2014]. The computed waveforms reproduce the amplitude and phase quite well for at least an hour. The frequency components of a far-field tsunami reflect the width and length of the fault as well as nonlinear interactions of the dominant wave components across the ocean. The alignment of the spectral peaks of the computed and recorded data thus provide validation of the unilateral rupture model.

4. Discussion and Conclusions

The complementary sensitivity of the teleseismic and tsunami observations to the offshore slip process is dramatically demonstrated for the 2015 Illapel, Chile, earthquake. The joint modeling indicates that there was little coseismic slip south of the hypocenter, even though this region has several large aftershocks (Figure 1) and appears to be seismically fully coupled [*Métois et al*., 2012]. The radiated energy for the

Figure 4. Comparison of observations (black lines) with computed tsunami waveforms and spectra (red lines) from the preferred model at water-level stations used in iterative modeling. (a) Regional DART stations. (b) Local tide gauges. Good agreement of both amplitude and phase at the DART stations could be achieved by a number of model grids, but only the unilateral rupture model can match the first arrivals at the tide gauges.

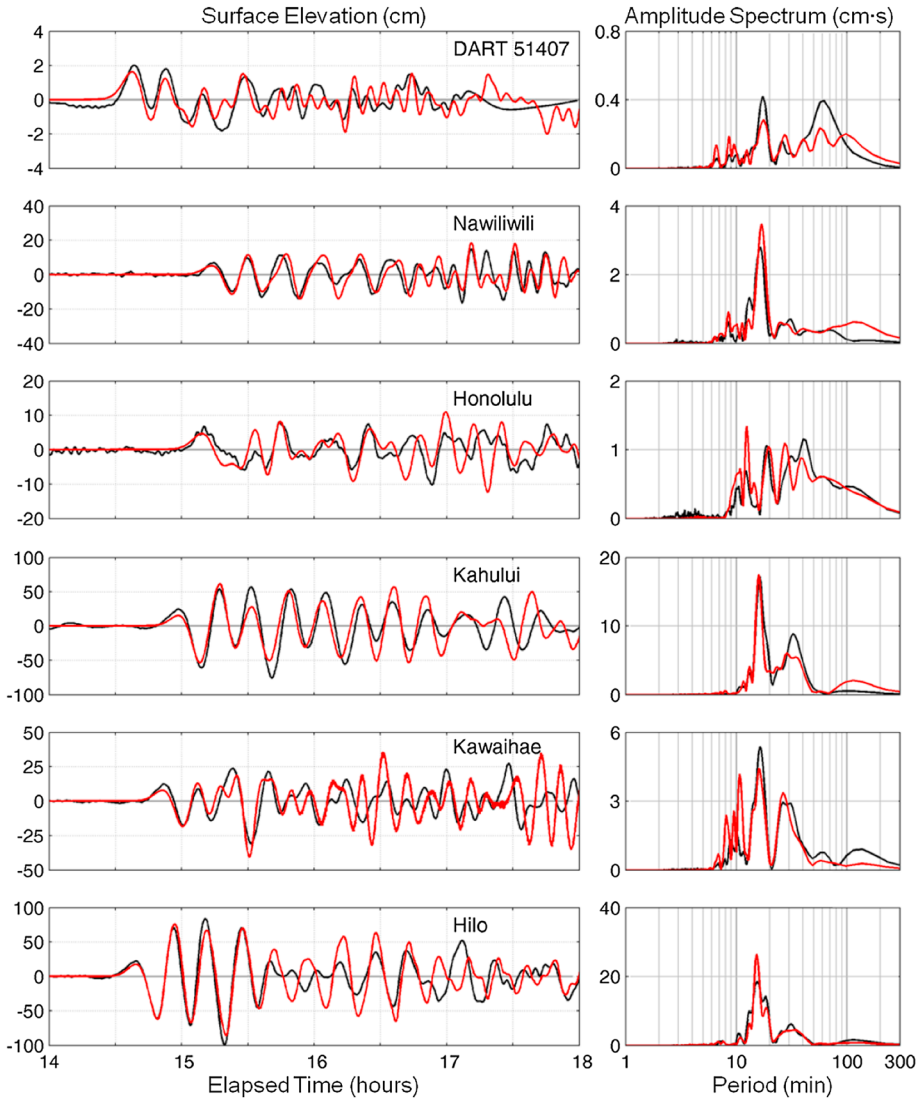

Figure 5. Comparison of observations (black lines) with computed tsunami waveforms and spectra (red lines) from the preferred model at DART 51407 and tide gauges in Hawaii. The computed waveforms are shifted later by 6 min to account for early arrivals of the modeled tsunami. These far-field data, which were not considered in the iterative approach, validate the preferred rupture model.

preferred model is 2.84×10^{16} J, obtained by the method described in *Ye et al.* [2016], which expands on the procedure of *Venkataraman and Kanamori* [2004]. The slip-weighted static stress drop estimate for the preferred model is 3.2 MPa (see *Ye et al.* [2016] for discussion), which is about 50% larger than for the earlier bilateral models as a result of the more localized rupture area.

The offshore region of large slip extends beyond the area of high-frequency bursts of *P* wave radiation, and there does appear to be some frequency dependence of radiation from the fault plane as found in other studies. The high-frequency radiation does support the unilateral northward overall slip distribution. However, the high-frequency distribution does not clearly define the large-slip zone. Additional constraints on the finite-fault spatial extent is provided by the tsunami observations with a good azimuthal distribution, which is only obtained in this case by inclusion of tide gauges along the Chile coast in combination with the DART stations.

The capability to model tsunami generation from rupture time histories is crucial in matching the fine details of the near-field observations. The regional DART observations provide constraints on the offshore placement

of the slip and the northern boundary. Even with low-resolution computation in the absence of detailed coastal bathymetry, comparison of the modeled and observed first arrivals at the local tide gauges allow iterative adjustment of the model grid extent to determine the southern boundary of the rupture. Thus, efforts to quickly incorporate tsunami observations into the finite-fault determinations will improve accuracy of the rapid slip model characterization. The far-field tsunami records in Hawaii that were not considered in the iterative adjustment of the model grid and parameters provide validation of the preferred model.

Acknowledgments

The IRIS DMS data center (http://www.iris.edu/hq/) was used to access the seismic data from Global Seismic Network and Federation of Digital Seismic Network stations. The DART and tide gauge data were downloaded from the NOAA National Data Buoy Center (http://www.ndbc.noaa.gov/) and CO-OPS Tsunami Capable Tide Stations (http://tidesandcurrents.noaa.gov/tsunami/). This data analysis made use of GMT, SAC, and Matlab software. This work was supported by NOAA grant NA15NWS4670025 to Kwok Fai Cheung and by NSF grant EAR1245717 to Thorne Lay. This is SOEST contribution 9610.

References

An, C., I. Sepúlveda, and P. L.-F. Liu (2014), Tsunami source and its validation of the 2014 Iquique, Chile earthquake, *Geophys. Res. Lett.*, *41*, 3988–3994, doi:10.1002/2014GL060567.

Aránguiz, R., et al. (2016), The 16 September 2015 Chile tsunami from the post-tsunami survey and numerical modeling perspectives, *Pure Appl. Geophys.*, *173*(2), 333–348, doi:10.1007/s00024-015-1225-4.

Bai, Y., K. F. Cheung, Y. Yamazaki, T. Lay, and L. Ye (2014), Tsunami surges around the Hawaiian Islands from the 1 April 2014 North Chile M_w 8.1 earthquake, *Geophys. Res. Lett.*, *41*, 8512–8521, doi:10.1002/2014GL061686.

Beck, S., S. Barrientos, E. Kausel, and M. Reyes (1998), Source characteristics of historic earthquakes along the central Chile subduction zone, *J. South Am. Earth Sci.*, *11*, 115–129.

Bretschneider, C. L., H. J. Krock, E. Nakazaki, and F. M. Casciano (1986), Roughness of typical Hawaiian terrain for tsunami run-up calculations: A user's manual, J.K.K. Look Lab. Rep., Univ. of Hawaii, Honolulu.

Cheung, K. F., Y. Bai, and Y. Yamazaki (2013), Surge around the Hawaiian Islands from the 2011 Tohoku tsunami, *J. Geophys. Res. Oceans*, *118*, 5703–5719, doi:10.1002/jgrc.20413.

Comte, D., A. Eisenberg, E. Lorca, M. Pardo, L. Ponce, R. Saragoni, S. K. Singh, and G. Suárez (1986), The 1985 central Chile earthquake: A repeat of previous great earthquakes in the region?, *Science*, *233*(4762), 449–453.

Contreras-López, M., et al. (2016), Field survey of the 2015 Chile tsunami with emphasis on coastal wetland and conservation areas, *Pure Appl. Geophys.*, *173*(2), 349–367, doi:10.1007/s00024-015-1235-2.

Hartzell, S. H., and T. H. Heaton (1983), Inversion of strong ground motion and teleseismic waveform data for the fault rupture history of the 1979 Imperial Valley, California, earthquake, *Bull. Seismol. Soc. Am.*, *73*(6A), 1553–1583.

Hayes, G. P., D. J. Wald, and R. L. Johnson (2012), Slab 1.0: A three-dimensional model of global subduction zone geometries, *J. Geophys. Res.*, *117*, B01302, doi:10.1029/2011JB008524.

Heidarzadeh, M., S. Murotani, K. Satake, T. Ishibe, and A. R. Gusman (2016), Source model of the 16 September 2015 Illapel, Chile, M_w 8.4 earthquake based on teleseismic and tsunami data, *Geophys. Res. Lett.*, *43*, 643–650, doi:10.1002/2015GL067297.

Kelleher, J. A. (1972), Rupture zones of large South American earthquakes and some predictions, *J. Geophys. Res.*, *77*(11), 2087–2103, doi:10.1029/JB077i011p02087.

Kikuchi, M., and H. Kanamori (1982), Inversion of complex body waves—III, *Bull. Seismol. Soc. Am.*, *81*(6), 2335–2350.

Lay, T., Y. Yamazaki, C. J. Ammon, K. F. Cheung, and H. Kanamori (2011), The 2011 M_w 9.0 off the Pacific coast of Tohoku Earthquake: Comparison of deep-water tsunami signals with finite-fault rupture model predictions, *Earth Planets Space*, *63*(7), 797–801, doi:10.5047/eps.2011.05.030.

Lay, T., L. Ye, H. Kanamori, Y. Yamazaki, K. F. Cheung, and C. J. Ammon (2013a), The February 6, 2013 M_w 8.0 Santa Cruz Islands earthquake and tsunami, *Tectonophysics*, *608*, 1109–1121.

Lay, T., L. Ye, H. Kanamori, Y. Yamazaki, K. F. Cheung, K. Kwong, and K. D. Koper (2013b), The October 28, 2012 M_w 7.8 Haida Gwaii underthrusting earthquake and tsunami: Slip partitioning along the Queen Charlotte Fault transpressional plate boundary, *Earth Planet. Sci. Lett.*, *375*, 57–70.

Melgar, D., et al. (2016), Slip segmentation and slow rupture to the trench during the 2015, M_w 8.3 Illapel, Chile earthquake, *Geophys. Res. Lett.*, *43*, 961–966, doi:10.1002/2015GL067369.

Métois, M., A. Socquet, and C. Vigny (2012), Interseismic coupling, segmentation and mechanical behavior of the central Chile subduction zone, *J. Geophys. Res.*, *117*, B03406, doi:10.1029/2011JB008736.

Munger, S., and K. F. Cheung (2008), Resonance in Hawaii waters from the 2006 Kuril Islands Tsunami, *Geophys. Res. Lett.*, *35*, L07605, doi:10.1029/2007GL032843.

Nishenko, S. P. (1985), Seismic potential for large and great interplate earthquakes along the Chilean and southern Peruvian margins of South America: A quantitative reappraisal, *J. Geophys. Res.*, *90*, 3589–3615, doi:10.1029/JB090iB05p03589.

Okada, Y. (1985), Surface deformation due to shear and tensile faults in a half space, *Bull. Seismol. Soc. Am.*, *75*(4), 1135–1154.

Saito, T., Y. Ito, D. Inazu, and R. Hino (2011), Tsunami source of the 2011 Tohoku-Oki earthquake, Japan: Inversion analysis based on dispersive tsunami simulations, *Geophys. Res. Lett.*, *38*, L00G19, doi:10.1029/2011GL049089.

Satake, K., et al. (2013), Tsunami source of the 2010 Mentawai, Indonesia earthquake inferred from tsunami field survey and waveform modeling, *Pure Appl. Geophys.*, 1–16, doi:10.1007/s00024-012-0536-y.

Tang, L., V. V. Titov, C. Moore, and Y. Wei (2016), Real-time assessment of the 16 September 2015 Chile tsunami and implications for near-field forecast, *Pure Appl. Geophys.*, *173*(2), 369–387, doi:10.1007/s00024-015-1226-3.

Tanioka, Y., and K. Satake (1996), Tsunami generation by horizontal displacement of ocean bottom, *Geophys. Res. Lett.*, *23*, 861–864, doi:10.1029/96GL00736.

Tsai, V. C., J. P. Ampuero, H. Kanamori, and D. J. Stevenson (2013), Estimating the effect of Earth elasticity and variable water density on tsunami speeds, *Geophys. Res. Lett.*, *40*, 492–496, doi:10.1002/grl.50147.

Venkataraman, A., and H. Kanamori (2004), Observational constraints on the fracture energy of subduction zone earthquakes, *J. Geophys. Res.*, *109*, B05302, doi:10.1029/2003JB002549.

Watada, S., S. Kusumoto, and K. Satake (2014), Traveltime delay and initial phase reversal of distant tsunamis coupled with the self-gravitating elastic Earth, *J. Geophys. Res. Solid Earth*, *119*, 4287–4310, doi:10.1002/2013JB010841.

Yamazaki, Y., and K. F. Cheung (2011), Shelf resonance and impact of near-field tsunami generated by the 2010 Chile earthquake, *Geophys. Res. Lett.*, *38*, L12605, doi:10.1029/2011GL047508.

Yamazaki, Y., Z. Kowalik, and K. F. Cheung (2009), Depth-integrated, non-hydrostatic model for wave breaking and run-up, *Int. J. Numer. Methods Fluids*, *61*(5), 473–497.

Yamazaki, Y., K. F. Cheung, and Z. Kowalik (2011a), Depth-integrated, non-hydrostatic model with grid nesting for tsunami generation, propagation, and run-up, *Int. J. Numer. Methods Fluids*, *67*(12), 2081–2107.

Yamazaki, Y., T. Lay, K. F. Cheung, H. Yue, and H. Kanamori (2011b), Modeling regional and remote tsunami observations with finite-fault slip models for the 11 March 2011 Tohoku earthquake (M_w 9.0), *Geophys. Res. Lett.*, *38*, L00G15, doi:10.1029/2011GL049130.

Yamazaki, Y., K. F. Cheung, G. Pawlak, and T. Lay (2012), Surges along the Honolulu coast from the 2011 Tohoku tsunami, *Geophys. Res. Lett.*, *39*, L09604, doi:10.1029/2012GL051624.

Yamazaki, Y., K. F. Cheung, and T. Lay (2013), Generation mechanism and near-field dynamics of the 2011 Tohoku tsunami, *Bull. Seismol. Soc. Am.*, *103*, 1444–1455, doi:10.1785/0120120103.

Ye, L., T. Lay, H. Kanamori, and K. D. Koper (2016), Rapidly estimated seismic source parameters for the 16 September 2015 Illapel, Chile M_w 8.3 earthquake, *Pure Appl. Geophys.*, *173*(2), 321–332, doi:10.1007/s00024-015-1202-y.

Yin, J., H. Yang, H. Yao, and H. Weng (2016), Coseismic radiation and stress drop during the 2015 M_w 8.3 Illapel, Chile megathrust earthquake, *Geophys. Res. Lett.*, *43*, 1520–1528, doi:10.1002/2015GL067381.

Yokota, Y., K. Koketsu, Y. Fujii, K. Satake, S. Sakai, M. Shinohara, and T. Kanazawa (2011), Joint inversion of strong motion, teleseismic, geodetic and tsunami datasets for the rupture process of the 2011 Tohoku earthquake, *Geophys. Res. Lett.*, *38*, L00G21, doi:10.1029/2011GL050098.

Yoshimoto, M., S. Watada, Y. Fujii, and K. Satake (2016), Source estimate and tsunami forecast from far-field deep-ocean tsunami waveforms—The 27 February 2010 M_w 8.8 Maule earthquake, *Geophys. Res. Lett.*, *43*, 659–665, doi:10.1002/2015GL067181.

Yue, H., T. Lay, L. Rivera, Y. Bai, Y. Yamazaki, K. F. Cheung, E. M. Hill, K. Sieh, W. Kongko, and A. Muhari (2014a), Rupture process of the 2010 M_w 7.8 Mentawai tsunami earthquake from joint inversion of near-field hr-GPS and teleseismic body wave recordings constrained by tsunami observations, *J. Geophys. Res. Solid Earth*, *119*, 5574–5593, doi:10.1002/2014JB011082.

Yue, H., T. Lay, L. Rivera, C. An, C. Vigny, X. Tong, and J. C. Báez Soto (2014b), Localized fault slip to the trench in the 2010 Maule, Chile M_w 8.8 earthquake from joint inversion of high-rate GPS, teleseismic body waves, InSAR, campaign GPS, and tsunami observations, *J. Geophys. Res. Solid Earth*, *119*, 7786–7804, doi:10.1002/2014JB011340.